Research Article

International Journal of
Protective Structures

International Journal of Protective Structures
1–27

DOI: 10.1177/20414196211035486
journals.sagepub.com/home/prs


Ballistic impact resistance of additive manufactured high-strength maraging steel: An experimental study

Miguel Costas[1], Maisie Edwards-Mowforth[2], Martin Kristoffersen[1], Filipe Teixeira-Dias[2], Vegard Brøtan[3], Christian O. Paulsen[1] and Tore Børvik[1]

Abstract

Maraging steel is a low carbon steel known for its ultra high-strength after heat treatment. In combination with Additive Manufacturing (AM), the properties of maraging steel indicate potential to enable complex geometries and improved performance-to-weight ratios for ballistic protection. This study investigates the ballistic performance of AM maraging steel monolithic plates and profile panels fabricated by powder bed fusion. The mechanical properties of the maraging steel, both in the as-built state and after heat treatment, were revealed through quasi-static and dynamic tests in three different directions with respect to the build direction. Metallurgical studies were also conducted to investigate the microstructure of the material both before and after testing. The ballistic perforation resistance of the maraging steel samples was disclosed in a ballistic range by firing 7.62 mm APM2 bullets towards the different target configurations. Ballistic limit curves and velocities were obtained, demonstrating that the thickest heat-treated AM maraging steel plate has a particularly good potential for ballistic protection. The hard core of the armour piercing bullet broke in all tests and occasionally shattered during tests with heat-treated targets. However, due to the severe brittleness of the material, the targets showed significant fragmentation in some cases and most significantly for the profile panels.

Keywords

Maraging steel, additive manufacture, lightweight protection, ballistic limit, heat treatment, metallurgical studies

Introduction

Research has shown that the ballistic perforation resistance of steel plates is an almost linear increasing function of the material's yield strength (Børvik et al., 2009). Thus, the use of advanced

[1]NTNU, Trondheim, Sor-Trøndelag, Norway
[2]The University of Edinburgh, Edinburgh, UK
[3]SINTEF Manufacturing, Trondheim, Norway

Corresponding author:
Miguel Costas, NTNU, Richard Birkelands veg 1A, Trondheim, Sor-Trondelag 7491, Norway.
Email: miguel.costas@ntnu.no

high-strength materials with optimal ballistic capacity can lead to improvements in the performance-to-weight ratio of monolithic armour plates (Demir et al., 2008; Kasilingam et al., 2019; Madhu and Bhat, 2011; Ranaweera et al., 2020). Historically, the light-weighting of armour systems has relied on areal density reduction, which after a certain level must be reinforced with advanced materials to achieve the necessary ballistic capacity. Materials with high strength have, however, typically less flexible manufacturing methods, limiting the opportunity for complex geometry and areal density reduction (Børvik et al., 2005). In recent years Additive Manufacturing (AM), a fabrication process based on the successive addition of material layer by layer, has introduced capacity for weight-saving intricate geometries to advanced materials. AM possesses a large unrealised potential in the field of ballistic protection, with the largest drawback being the uncertainty surrounding the mechanical properties of AM materials under impulsive loading. Promisingly, a recent study by Kristoffersen et al. (2020) demonstrated marginal discrepancy in ballistic response between AM and traditionally die-cast aluminium plates.

Novel metal AM processes developed by for example Vyatskikh et al. (2018) are able to achieve complex geometries with a resolution in the nano-scale. However, the most common AM techniques for metallic materials, powder bed fusion (PBF) and direct energy deposition (DED), produce components with unit cell sizes in the range 10–100 μm. PBF and the subcategory selective laser melting (SLM) involve the local melting of metallic powder with a high energy laser directly from a computer-aided design (CAD) file. The process is controlled by parametres such as laser power, laser speed and powder particle diametre that are fine-tuned to produce parts with comparable or often superior mechanical properties to traditional manufacturing methods (Akram et al., 2018; Frazier, 2014; Vock et al., 2019). This can be attributed to the fine grain structure left by laser melt pools of diametre close to 1 μm formed by exceptionally high cooling rates (from 10^3 to 10^8 K/s (Jägle et al., 2014)). In the literature, the optimisation of low density AM metallic lattice structures that demonstrate a high capacity for dynamic energy absorption is an increasingly popular subject for exploration. Harris et al. (2017) set out to measure the effects of AM-induced microstructure on the resulting mechanical performance. The understanding of the relationship between microstructure and impact response is similarly critical for ballistic impact scenarios and other fields where metal AM applications are consequential. These are prominently the aerospace, tooling and defence industries, where AM has opened up new possibilities for high performance, lightweight components with complex geometries (Ngo et al., 2018). The AM technology also opens the possibility of combining multiple materials to form even more impact resistant structures (Masood et al., 2018). High-speed loading conditions are relevant for AM applications within defence and aerospace in particular. In addition to low areal density, this makes obtaining a favourable compromise between mechanical strength and ductility sought after.

The material most commonly used for AM in aerospace and tooling products is maraging steel, known for its superior strength and hardness with reduced loss of toughness and malleability. Maraging steel is a special class of low-carbon steel with characteristics that make it particularly well suited to AM techniques. For example, the high cooling rates imposed by PBF that give AM maraging steel optimal strength would cause extreme hardness and breakages in high carbon steels (Tan et al., 2017). The mechanical properties of SLM maraging steel substantially improve after heat treatment. After the industry standardised heat treatment of 490 °C for 6 h, the micro-hardness and tensile strength significantly increase and as a consequence the fracture elongation and impact toughness are reduced (Bai et al., 2019). The compromise of heat-treating AM maraging steel is therefore obtaining ultra high-strength while worsening ductility. This effect is well established and is consistent throughout the many studies conducted, however, the effect of specific temperature and duration of heat treatment on ductility are debated in the literature (Bai et al., 2019; Jägle et al., 2014, 2016; Tan et al., 2017). Furthermore, it has been shown that laser scanning speed and

Table 1. Chemical composition of the 1.2709 maraging steel powder.

Element	Al	C	Co	Cr	Fe	Mn	Mo	N	Ni	O	P	S	Si	Ti
Min. wt %	–	–	8.5	–	Balance	–	4.5	–	17.0	–	–	–	–	0.8
Max. wt %	0.1	0.03	10.0	0.25	Balance	0.15	5.2	0.10	19.0	0.10	0.01	0.01	0.1	1.2

layer thickness have significant impact on the hardness and relative density of the finished product (Kempen et al., 2011).

The superior mechanical strength achieved after heat treatment makes AM maraging steel a strong candidate for protection against ballistic impact. The apparent potential to optimise for ductility through heat treatment while retaining ultra high tensile strength is an exciting prospect for this application and does not seem to have been explored yet. It is also proposed that the freedom associated with AM fabrication could transform the weight efficiency of protective components against small-arms projectiles. Also, on-site repair or reinforcement made possible with flexible AM methods could improve adaptability and safety of for example overseas operations (Børvik et al., 2008a, 2008b; Ma and Liew, 2013; Ngo et al., 2018).

It was therefore the aim of this study to investigate AM maraging steel under ballistic impact where it is subjected to large strains, high strain rates and possible temperature softening due to self-heating. Particular attention was paid to the effect of heat treatment on the material's mechanical behaviour and ductility. To this end, ballistic impact tests were carried out on a number of as-built and heat-treated AM plates of two different thicknesses and truss-like components. The results from these tests were reported and supported by both an examination of the microstructure of the material and a comprehensive programme of material characterisation tests at different strain rates. It was found that the thickest heat-treated maraging steel plate had a great potential in ballistic protection. The hard core of the APM2 bullet broke in all tests, and in some of the tests it shattered completely. However, due to the severe brittleness of the material, the targets showed significant fragmentation in some cases, and most so for the profile plates. Thus, more work is required in order to increase the ductility of AM maraging steel targets through a proper heat treatment before it can be used with confidence in ballistic protection, but the potential for such solutions was found to be significant.

Materials

Maraging steel 1.2709

Maraging steels are iron-nickel alloys well suited for AM. The most common alloy, 1.2709, is offered by all metal AM machine manufacturers and several metallurgical companies. The chemical composition of this powder is listed in Table 1. 1.2709 maraging steel is relatively soft (30–35 HRC) in its solution annealed state, but a hardness in the range of 48–58 HRC can be obtained through ageing. It can be polished and nitrated to achieve fine surface structures and increased surface hardness, and coated using chemical vapour deposition (CVD). The material has low thermal expansion ($\sim 10\ \mu m/(m°C)$) , good resistance to thermal cracking and offers good weldability. Crack propagation in maraging steel is slower than for similarly strong carbon steel, which makes the material well suited for safety critical parts that require high strength and damage tolerance, referred to as high toughness. The material is used both in cold and hot applications. The good malleability in solution annealed state allows the steel to be cold rolled into thinner skins than other steels with similar strength. This makes the material attractive for its main application, which is

lightweight aircraft components. In addition to shell constructions, the material is used for structural parts that require high damage tolerance, for example aircraft landing gear, helicopter undercarriages and machine parts such as crankshafts and gears. AM supports new unique design possibilities for this high-strength steel.

Maraging steels derive their strength not from carbon content, but from providing a high number density of nanometre-sized intermetallic precipitates in a martensitic matrix (Casati et al., 2016; Jägle et al., 2014). Conde et al. (2019) reported that as-built 1.2709 has a non-homogeneous microstructure with 4 vol% retained austenite and no discernible secondary precipitation. The AM parts demonstrated higher hardness than the non-AM parts, however, the cyclic heating during the building process clearly is not sufficient to nucleate significant precipitate formation. Subsequent ageing is thus necessary to provide the hardest condition with the highest strength.

Casati et al. (2016) evaluated the effect of ageing temperature and duration on tensile performance. The tests revealed that the ageing process dramatically increases strength while ductility falls compared with the as-built samples. It is suggested, however, that over-ageing leads to martensite-to-austenite reversion and to a decrease in mechanical strength. Therefore, the ageing procedure appears to be more sensitive to temperature than time, a conclusion supported by other sources (Bai et al., 2017; Casati et al., 2016; Kempen et al., 2011; Mooney et al., 2019; Tan et al., 2017; Yasa et al., 2010). A further option of solution annealing at 980 °C for 1 h is shown to reduce austenite retention and increase homogeneity in the material. Grain growth is, however, introduced under these conditions (Casati et al., 2016) and it has been suggested that this may lead to improved ductility, although reduced tensile strength (Tan et al., 2017) and reduced impact toughness (Bai et al., 2017).

Yin et al. (2018) found that under-ageing could increase the tensile ductility, albeit at the cost of a decrease in the tensile strength. It was shown that an under-aged AM 1.2709 part will exhibit full hardness after just over 1 h at 490 °C. However, this finding is not fully consistent with other reports, which could be due to production parametres. Contrary to the above, Mooney et al. (2019) claimed that a compromise between strength and ductility is reached after 6–8 h at 525 °C. It is suggested that over-ageing is the best way to achieve the optimum compromise between strength and ductility.

Material production

For this study, maraging steel specimens were built using the SLM technique (ISO/ASTM. 52900:2018:-06, 2018) and 300 grade Fe-18Ni-300 (1.2709) powder with a particle size between 10 and 45 μm, from LPW Technology. A Concept Laser M2 with 200 W Yb:YAG fibre laser was used with a nitrogen shielding gas of purity above 99.9%. The build performed an island scan strategy, melting 5 mm × 5 mm squares in a randomised order and shifting scan direction by 90° for each layer. Additionally, a 1 mm scan pattern shift in the x and y directions was applied to each layer. Figure 1 illustrates the laser movement in sequential layers according to this strategy, while Table 2 displays the properties of the manufacturing process.

Three different renditions of SLM manufactured grade 300 (1.2709) maraging steel specimens were produced. These are monolithic 100 mm × 100 mm plates of 5 and 10 mm thickness, and a profile plate with the same areal density as the 10 mm thick plate (see Figure 2). Note that the geometry of these profile plates was not optimised. Post SLM, half of the specimens of each type underwent a 6 h heat treatment at 490 °C before cooling to room temperature in air. This heat treatment is the industry standard, and has shown to be the most reliable method for high tensile strength (Casati et al., 2016). It should be noted that around a quarter of the way through the fabrication process, the machine was stopped to replenish powder supplies. The pause during which the laser was not heating the specimens caused cooling of the already built material, and thus a small notch formed on the surface of each plate, hereafter referred to as the ‘print-stop line’.

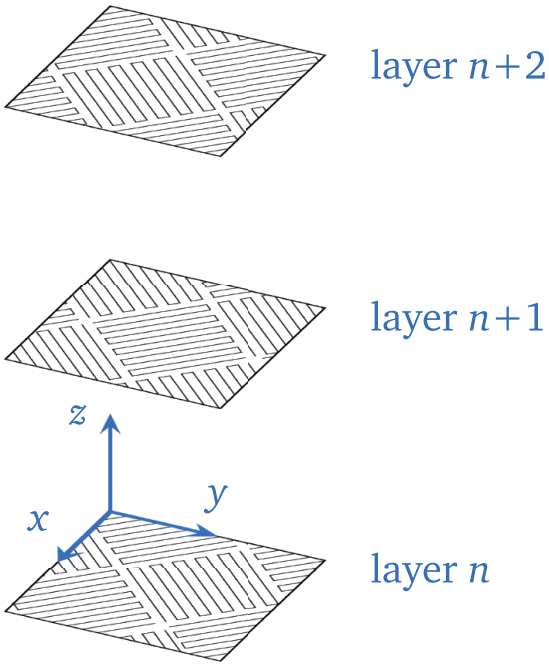

Figure 1. The applied build strategy for all specimens, showing the laser paths for three subsequent layers. The island pattern makes up the bulk of the part, and thereafter a contour path completes the outer surface layer. The layer thickness is 30 μm in this study.

Table 2. Properties of SLM manufacturing process.

Laser power (W)	Layer thickness (μm)	Laser velocity (mm/s)	Focus diametre (μm)	Hatch distance (μm)
180	30	600	150	105

Metallurgical studies

The microstructure of both the as-built and the heat-treated materials was investigated with a Zeiss Ultra 55 Limited Edition Field Emission scanning electron microscope (SEM) and a Leica MEF4M optical microscope (OM). The samples were prepared by mechanical grinding and polishing to 1 μm, followed by either etching for 2 min in 2% Nital (Zipperian, 2010) or vibration polishing. For the latter, the samples were polished using a VibroMet2 from Buehler for 12 hours to remove the final deformation layer. The suspension used with the vibration polisher had pH 8 and contained SiO_2 particles with a size of 0.02 μm. Finally, after the final polishing step, all samples were rinsed in an ultrasonic acetone bath for 5 minutes to obtain a clean surface finish. The etched samples were used for imaging in the SEM using secondary electron mode, while the vibration polished samples were used for OM imaging and electron backscatter diffraction (EBSD).

Figure 3 shows a comparison between as-built samples (shown on the left) and the heat-treated samples (shown on the right) of the maraging steel in all directions. The build direction was defined as PD (or z in Figure 2(a)) and gives a top view of the printed strings. In both the normal direction ND (or x in Figure 2(a)) and the transverse direction TD (or y in Figure 2(a)), a front view and a

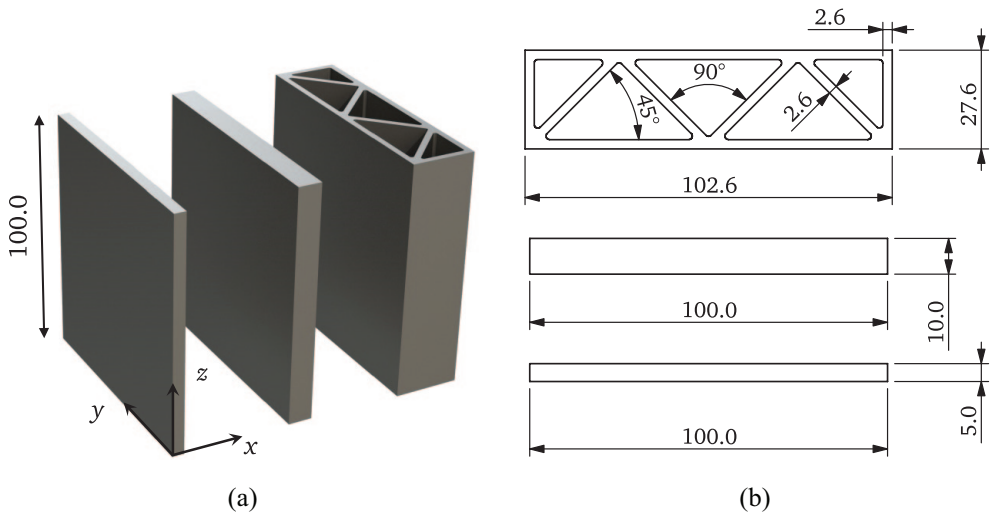

Figure 2. Geometry of AM maraging steel plates used in the ballistic impact tests, where: (a) shows a 3D render with the coordinate system and (b) the cross-sectional geometries of the plates (all linear dimensions in mm).

side view of the printed strings are shown. Figure 3(a) shows OM images of the polished surface. The black 'circles' are pores in the fabricated material of a wide range of sizes. The honeycomb-like structure and boundaries between melt tracks can be seen in the SEM image (Figure 3(b)) of the as-built samples, as the material was built up in layers. Figure 3(c) shows inverse pole figure (IPF) maps obtained by EBSD and shows the grain structure inside the scan tracks. The IPF maps were acquired using a step size of 0.5 μm. The colours correspond to a grain orientation given by the legend in the centre of the figure. No significant differences are observed when comparing the as-built samples and the heat-treated samples.

Material testing

The as-built and heat-treated materials were both tested in quasi-static uniaxial tension, while only the as-built material was tested at elevated strain rates for the reasons set out below. Tensile specimens with the dimensions given in Figure 4(a) were machined from a 5 mm thick AM maraging steel plate at 0°, 45° and 90° with respect to the build direction (see Figure 4(b)) using spark erosion and a lathe. No tests were carried out in the thickness direction. However, an example of such experiments can be found in Forrestal et al. (2014). The diametres of the gauge area of each specimen were measured before testing with a precision caliper and were found to be within 0.02 mm of the nominal 3 mm. An overview of the material and component tests is sketched in Figure 5.

Quasi-static tests were conducted at room temperature using an Instron 5982 universal testing machine at 0.3 mm/min, leading to an initial strain rate of 1×10^{-3} s^{-1} in the specimen's gauge area. During testing, two synchronised Basler acA4112-30um cameras were used to record the specimen from two orthogonal angles at 2 frames per second with a resolution of 12.3 megapixels. Care was taken to ensure maximum contrast between the specimen and the bright background and that the orientation of the specimen was consistent across all tests, in that the original plate thickness was orthogonal to one of the cameras' angle. Edge tracing using the in-house software eCorr (Fagerholt

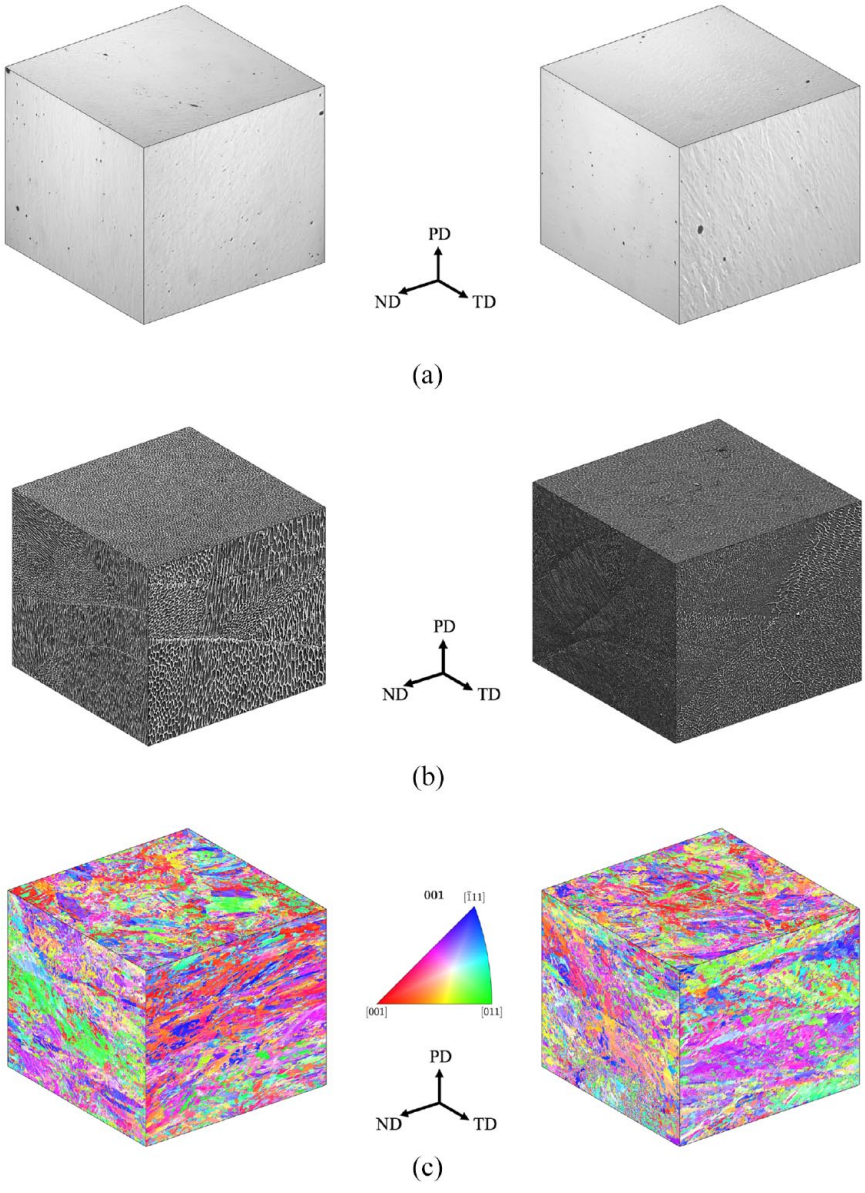

Figure 3. Cubes illustrating the microstructure of the as-built (left) and the heat-treated (right) AM maraging steel in different directions: (a) OM images of a polished sample, (b) SEM images of an etched sample and (c) inverse pole figure (IPF) maps acquired by EBSD where colours are indicative of grain orientation.

et al., 2013) was run on the images to obtain the current minimum diametre in each frame, enabling computation of the current cross-sectional area A as

$$A = \frac{\pi D_{\mathrm{ND}} D_{\mathrm{TD}}}{4} \tag{1}$$

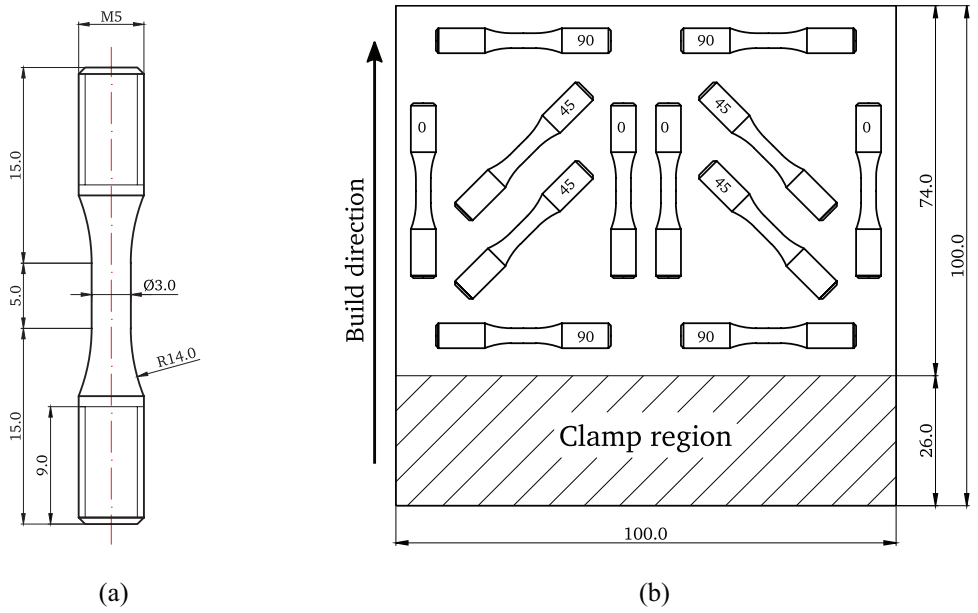

Figure 4. (a) Specimen geometry and (b) extraction scheme from a 5 mm thick plate at 0°, 45° and 90° with respect to the build direction (linear dimensions in mm).

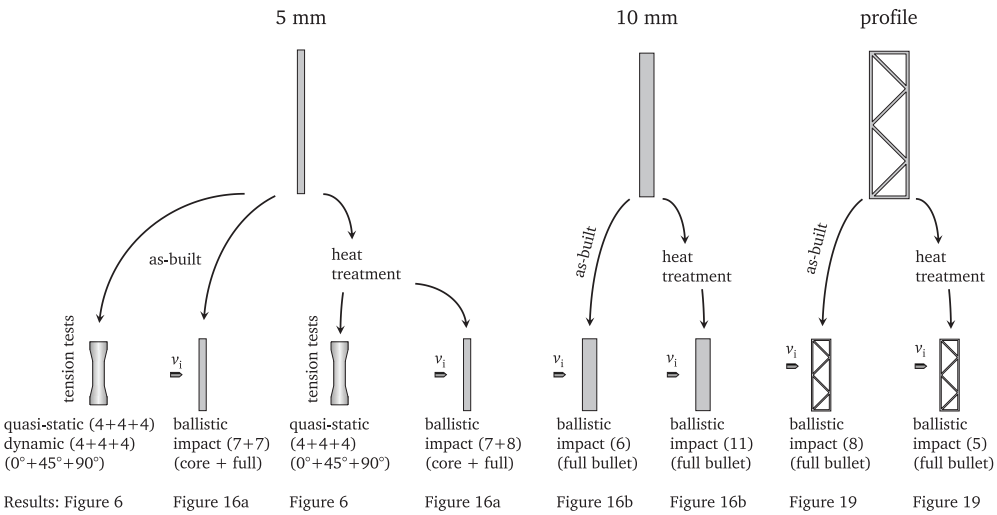

Figure 5. Overview of experimental programme, where the number in parenthesis indicate the number of tests for each case. All tension test specimens were machined from the 5 mm plates, and all plates from Figure 2 were subjected to ballistic impact.

where D_{ND} and D_{TD} are the diametres measured in the normal and transverse directions to the thickness of the original plate, respectively. Both quantities differed to some extent owing to the modest anisotropic plastic strains developed during the test. Assuming incompressible plastic deformation, the Cauchy (true) stress σ and the logarithmic (true) strain ε can be readily obtained as

Table 3. Key results from quasi-static tensile tests.

Material	Direction	Test	$\sigma_{0.2}$ (MPa)	S_{UTS} (MPa)	e_{UTS} (–)	ε_{frac} (–)	σ_{max} (MPa)
As-built	0°	1	1167.7	1166.7	0.0141	0.2672	1320.8
		2	1045.7	1065.3	0.0160	0.1953	1155.8
		3	1046.7	1093.9	0.0115	0.0122	1107.3
		4	1122.3	1116.1	0.0090	0.0416	1141.3
	45°	1	1103.4	1217.4	0.0310	0.2948	1362.7
		2	1155.6	1177.8	0.0199	0.0688	1232.1
		3	988.7	1157.8	0.0363	0.1913	1261.2
		4	1175.8	1190.5	0.0241	0.0685	1245.2
	90°	1	1059.8	1184.9	0.0545	0.9015	1652.3
		2	1029.9	1158.5	0.0423	0.6633	1478.3
		3	1147.8	1173.8	0.0438	0.7933	1586.3
		4	1112.7	1174.2	0.0493	0.7270	1536.2
Heat-treated	0°	1	1897.6	2041.1	0.0190	0.0253	2083.9
		2	1968.1	1954.5	0.0148	0.0147	1983.5
		3	2065.7	2072.5	0.0192	0.1233	2164.4
		4	1924.2	1948.0	0.0129	0.0133	1973.8
	45°	1	2048.6	2142.2	0.0177	0.0683	2200.2
		2	1989.6	1986.0	0.0167	0.0216	2024.5
		3	1989.7	2048.3	0.0214	0.0297	2097.0
		4	2017.2	2013.5	0.0188	0.0458	2060.6
	90°	1	1931.1	2010.6	0.0183	0.2214	2191.6
		2	2004.8	2001.0	0.0171	0.1910	2167.6
		3	2016.2	1994.4	0.0142	0.0186	2027.8
		4	1970.9	2052.4	0.0202	0.1511	2175.6

$$\sigma = \frac{F}{A} \quad \text{and} \quad \varepsilon = \ln\left(\frac{A_0}{A}\right) \tag{2}$$

where F is the force obtained from the load cell and A_0 is the initial cross-sectional gauge area of the specimens. The plastic strains ε^{p} can then be computed as $\varepsilon^{\mathrm{p}} = \varepsilon - \sigma / E$, where E is the elastic modulus. Table 3 lists some key results from the tensile tests; the 0.2% proof stress $\sigma_{0.2}$, the ultimate tensile strength S_{UTS} (peak force divided by A_0), the engineering strain at peak force e_{UTS}, the fracture strain $\varepsilon_{\mathrm{frac}} = \ln(A_0 / A_{\mathrm{frac}})$ where A_{frac} is the cross-sectional area at fracture, and the maximum true stress σ_{max}.

Figure 6(a) shows the quasi-static true stress-strain curves of the as-built and heat-treated material in the three tested directions, with four repetitions in each direction. On the one hand, and in spite of a considerable scatter in the results, it can be clearly observed that after heat treatment the initial yield stress of the material is almost doubled, reaching values above 2 GPa. On the other hand, the ductility of the heat-treated material was significantly reduced compared with that of the as-built samples, especially in the 90° direction.

Whilst the scatter made it difficult to extract robust conclusions, it appeared that the initial yield stress of the as-built material was not isotropic. Indeed, tests in the build direction seemed to yield earlier than those in the 45° or 90° directions, although the results were also more dispersed. The

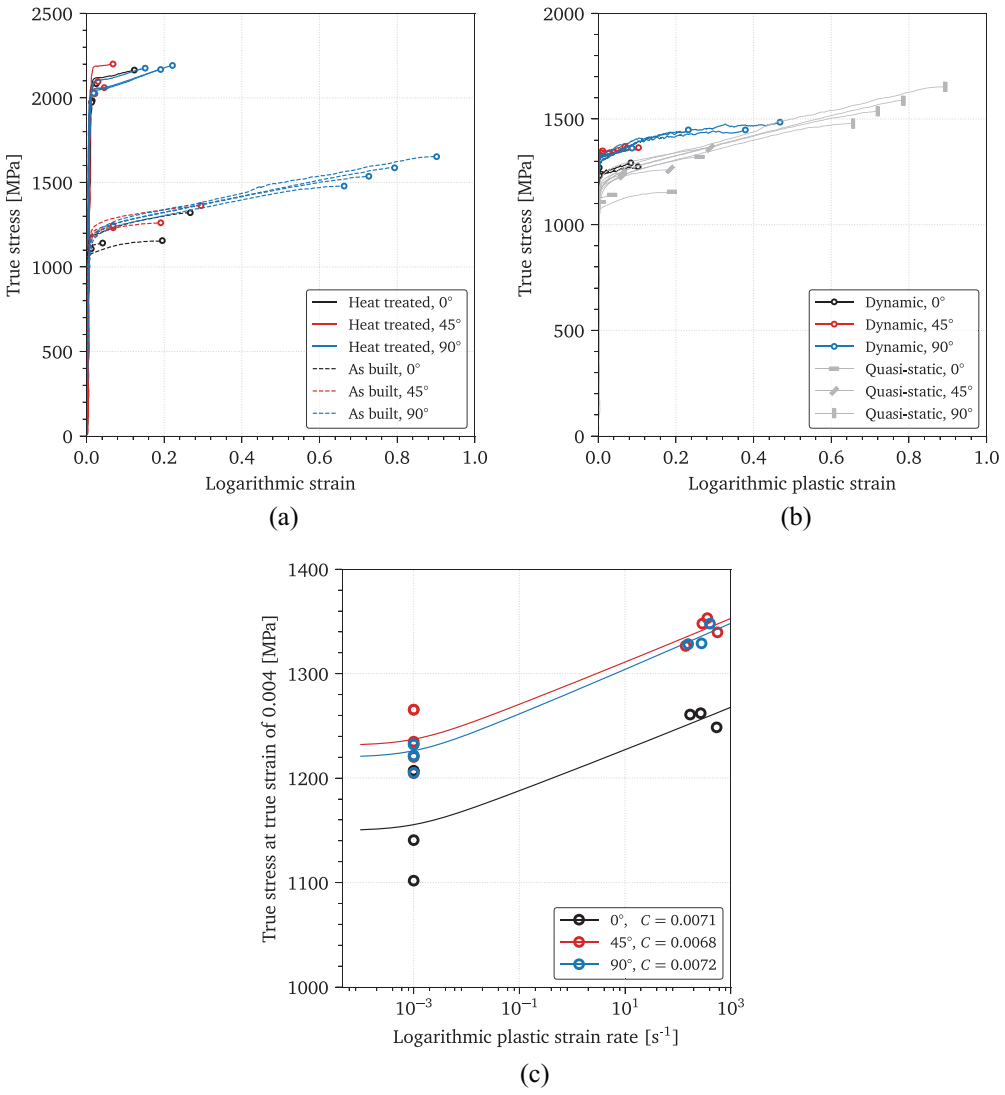

Figure 6. Results from quasi-static and dynamic tensile tests on AM maraging steel specimens: (a) true stress-logarithmic strain curves from quasi-static tensile tests, (b) true stress-logarithmic plastic strain curves from SHTB tests of as-built specimens only (compared with the corresponding quasi-static curves in grey) and (c) true stress-logarithmic plastic strain rate curves from quasi-static and SHTB tests at a true plastic strain of 0.04.

anisotropy in the failure strain was clearer, and the material showed a much higher ductility in the orientation orthogonal to the build direction than in the other two tested directions. In line with these results, tensile specimens in the 90° direction exhibited noticeable necking before failure. This is illustrated in Figure 7, where the most brittle (0°) and most ductile (90°) specimens are shown immediately before fracture occurred in the quasi-static tensile tests.

Ductility was significantly reduced after heat treatment. Some heat-treated specimens developed only marginal plastic strains before failure regardless of their orientation. The most

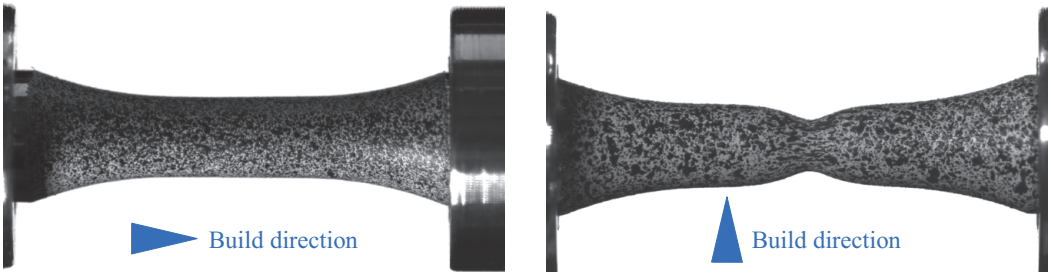

Figure 7. Images of: (a) the most brittle and (b) the most ductile specimens immediately before fracture in the quasi-static tensile tests. These specimens were extracted at 0° and 90° with respect to the built direction, respectively.

considerable reduction was observed in the specimens orthogonal to the build direction, where strains at failure dropped from 0.77 to 0.15.

SEM fractographies of the tensile specimens supported the assessment of the difference in ductility of the as-built and heat-treated samples. Figure 8(a) shows a typical as-built 0° sample with numerous voids spread across the fracture surface, which reduce the ductility. Conversely, the as-built 90° sample in Figure 8(b) had mostly a dimpled fracture surface, with some large voids from particles and cracks. Such a dimpled fracture surface indicates ductile fracture. Fractographs of the heat-treated samples showed signs of quasi-brittle, cleavage-type fracture that were not present in the as-built specimens. From the fracture surfaces of the heat-treated samples in Figure 8(c) and (d) little difference was seen between the orientations, and both surfaces showed dimples in the centre of the specimens, albeit less than in Figure 8(b).

Dynamic split-Hopkinson tension bar (SHTB) tests were conducted to characterise the material at elevated strain rates. Since the strain rate sensitivity is known to be low in ultra high-strength steels (Børvik et al., 2009), these tests were conducted on the as-built material exclusively. Seventeen specimens were tested with four successful tests for each of the directions 0°, 45° and 90° at strain rates ranging from 140 to 670 s^{-1}. True strains were computed by edge tracing in the same fashion as for the quasi-static tests. A Phantom v2511 high-speed camera was placed on one side of the specimen and an Opto Engineering telecentric illuminator, generating monowavelength collimated light beams, was placed on the opposite side in such a way that the outline of the specimen could be easily identified. The true stress was then computed based on the measured minimum diametre and the force obtained from the strain gauges attached to the bars using classical stress wave theory (Chen and Song, 2011; Chen et al., 2011). The true stress-logarithmic plastic strain curves from the SHTB tests are shown in Figure 6(b), where stresses are seen to be higher than those in the quasi-static tensile tests. Moreover, the tests in the direction orthogonal to the build direction showed a more accelerated work-hardening compared to their quasi-static equivalents.

The true stresses corresponding to a true plastic strain of 0.04 are plotted in Figure 6(c) for the quasi-static and dynamic tests, where the positive strain-rate sensitivity of the material can be clearly observed. The lines in the figure correspond to a best fit to a viscoplastic term in the form

$$\sigma|_{\dot{p}} = \sigma|_{\dot{p}_0}\left(1+\frac{\dot{p}}{\dot{p}_0}\right)^C \tag{3}$$

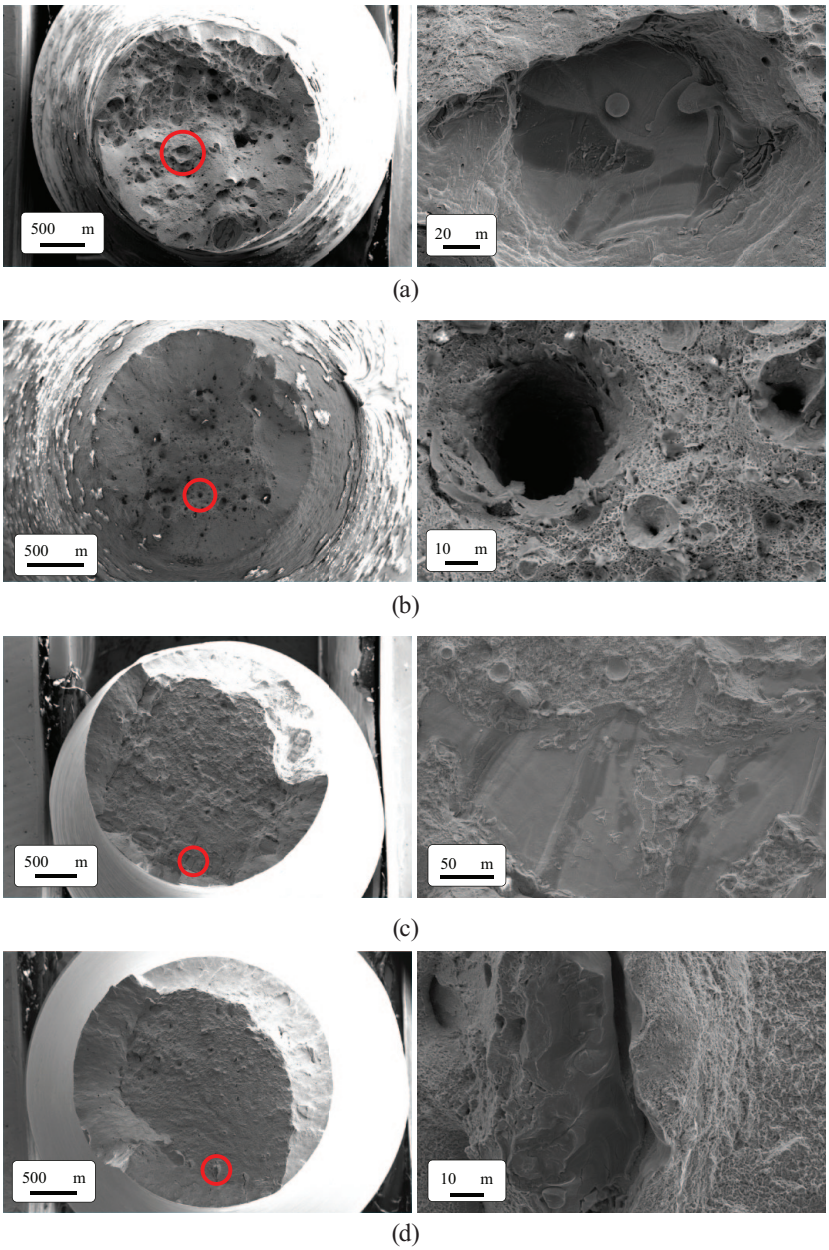

Figure 8. SEM images of fracture surfaces from quasi-static tensile tests: (a and b) show as-built 0° and 90°, respectively, while (c and d) show heat-treated 0° and 90°, respectively. The images on the right show a close up of the area marked with a red circle on the left image.

where $\sigma|_{\dot{p}}$ and $\sigma|_{\dot{p}_0}$ are the stresses at equivalent plastic strain rates of $\dot{p}$ and $\dot{p}_0$, respectively, and C is the strain rate sensitivity parametre. As shown in Figure 6(c), the identified values of C were approximately 0.007 for all three tested directions, a result which is similar to C values previously reported for other high-strength steels (Børvik et al., 2009).

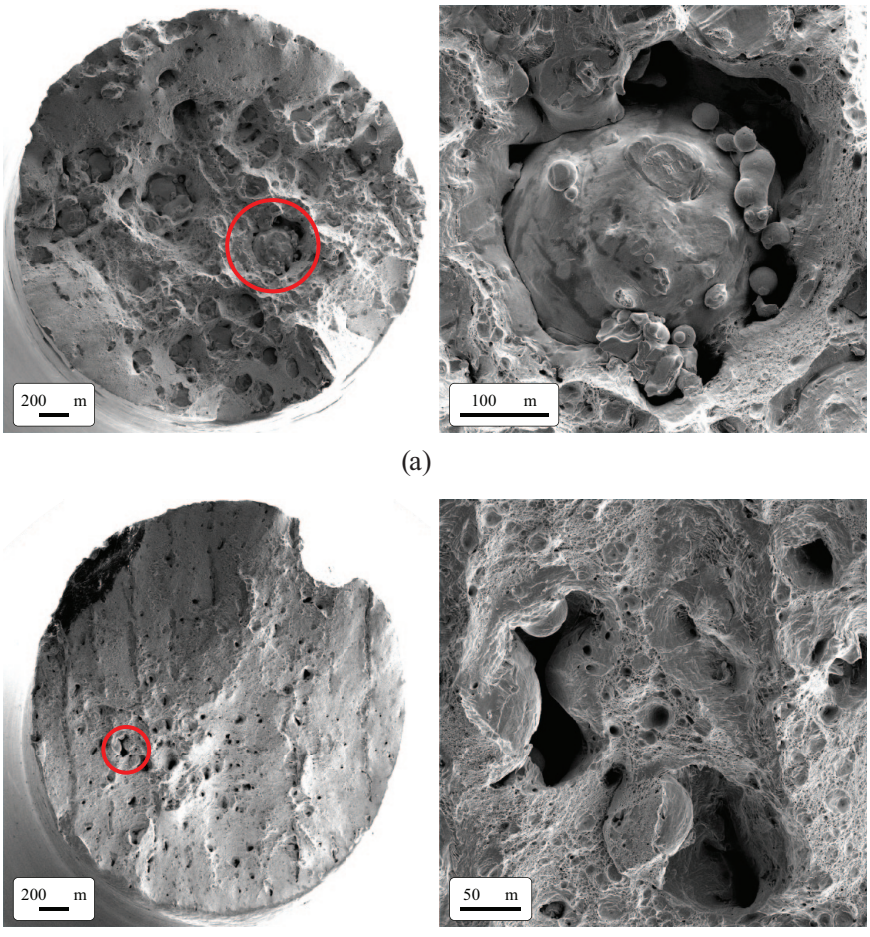

Figure 9. SEM images of the fracture surfaces from typical dynamic tensile tests on as-built specimens: (a) 0° and (b) 90°. The images on the right show a close up of the area marked with a red circle on the left image.

The resulting fracture surfaces from the dynamic tests are shown in Figure 9 for a representative sample at 0° and 90°. As seen from the curves in Figure 6(b), the samples at 90° were consistently more ductile also at high strain rates. This difference is illustrated by the fracture surfaces, which show that the 0° sample (Figure 9(a)) contained many more larger voids and defects compared with the 90° sample (Figure 9(b)). This was also consistent with what is shown in Figure 8.

The large particle decorated with a number of unmolten maraging steel powder particles shown in Figure 9(a) deserved more attention, mostly because particles of this size can be detrimental for the ductility of any metallic material. The diametre of the particle was approximately 300 μm, that is, roughly 10 times bigger than the powder particles used in the print. Thus, it was too large to be a part of the powder used and may be a result of micro-segregation (Gorsse et al., 2017; Kim et al., 2020). This problem may be due to an unusually high percentage of titanium and oxygen in some powder particles, which results in the rapid flow of titanium to the front of the melt pool during fabrication, leaving disproportionate concentrations of that element. Even with a very low

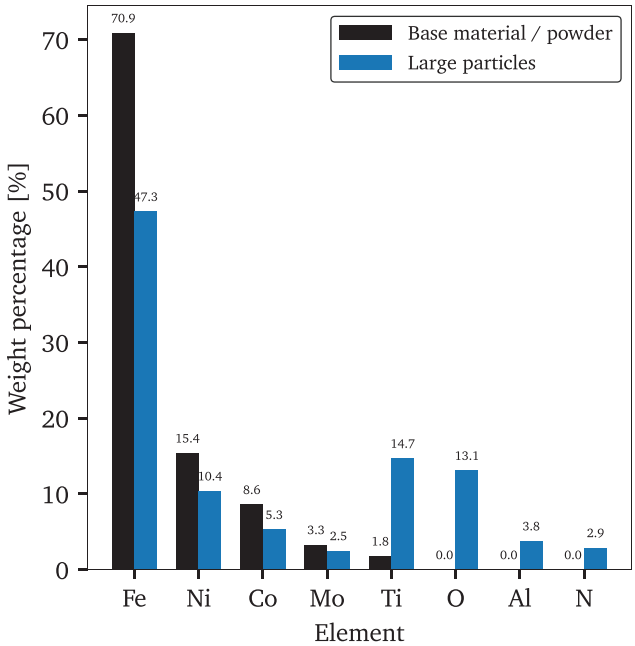

Figure 10. Comparison of the chemical composition of the base material and the large particles found in the material, obtained by EDS.

concentration of oxygen, oxidation can occur and leave brittle regions in the material that can lead to cracking. The chemical composition of these large particles and the base material were analysed under energy-dispersive X-ray spectroscopy (EDS) to support this argument. The results of the analyses plotted in Figure 10 clearly confirmed the high concentration of titanium and oxygen in the large particles compared to the base material.

To better understand the influence of the heat treatment on this large particle, one tensile test specimen was investigated in a Nikon XT H225 ST MicroCT machine. First, the as-built specimen was scanned and the locations of some of the larger particles in the gauge area were determined. Thereafter, the same specimen was heat-treated for 6 h at 490 °C, before it was re-scanned. Figure 11 shows the same specimen's cross section at the largest obtained particle both before and after heat treatment. As seen, these larger particles were unaffected by the heat treatment, and it can be concluded that the detrimental effect of the heat treatment on the ductility was not caused by growth of the larger particles.

Ballistic tests

Experimental set-up

The impact tests on the maraging steel plates were carried out in a ballistic range described in previous studies (Børvik et al., 1999, 2009; Kristoffersen et al., 2020). For this study, a smooth-bored Mauser gun with a barrel length of 1 m was used. The gun was enclosed within a sealed 16 m^3 test chamber and a magnetic trigger was used to allow firing from a safe distance. All plates were impacted by full size 7.62 mm APM2 bullets, each weighing 10.7 g, with the dimensions given in Figure 12. In addition, 14 of the 5 mm thick plates were impacted by the hard core only of the full

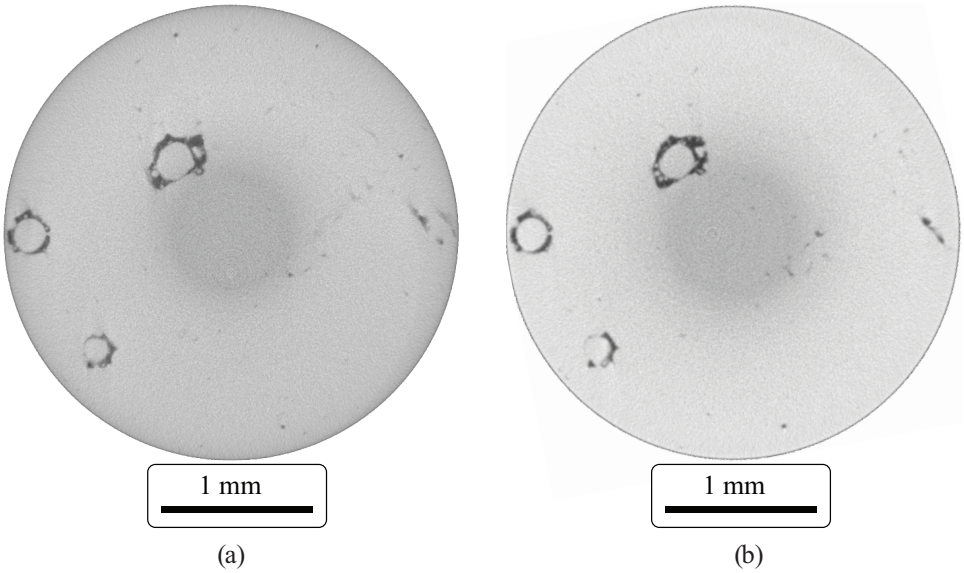

Figure 11. CT scans from the gauge area of a tensile test specimen: (a) as-built and (b) after heat treatment.

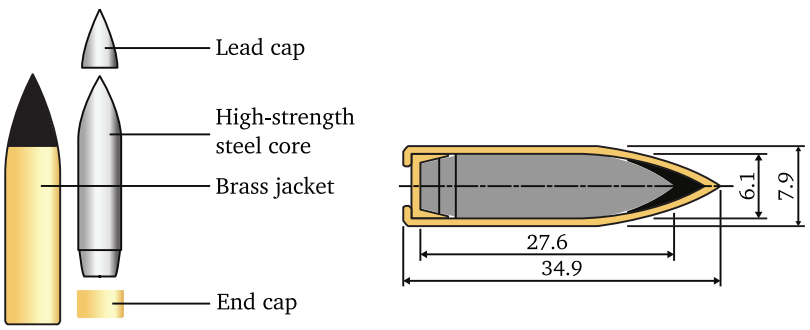

Figure 12. APM2 bullet used in tests (dimensions in mm).

bullet to investigate the effect of the casing on the perforation process. In these tests, the 6.1 mm diametre, 5.25 g mass, high-strength steel core of the APM2 bullet was inserted in a 0.3 g plastic sabot and fired from the same rifle. A Phantom v2511 high speed camera with a frame rate of 100,000 fps captured the impacts, with lighting by two Cordin 550 J flashlights and four MultiLED QT GSVitec lamp heads. Based on the high-speed videos, initial and residual bullet velocities (respectively v_i and v_r) were determined by applying a point tracking algorithm available in the in-house software eCorr (Fagerholt et al., 2013). An overview of the experimental programme can be found in Figure 5.

One edge of each plate was fastened with a steel clamp extending 26 mm from the edge as shown in Figure 4(b), leaving the remaining three edges unrestrained. The plates were aligned so that the bullet impacted the target with a 25 mm vertical distance between each shot,

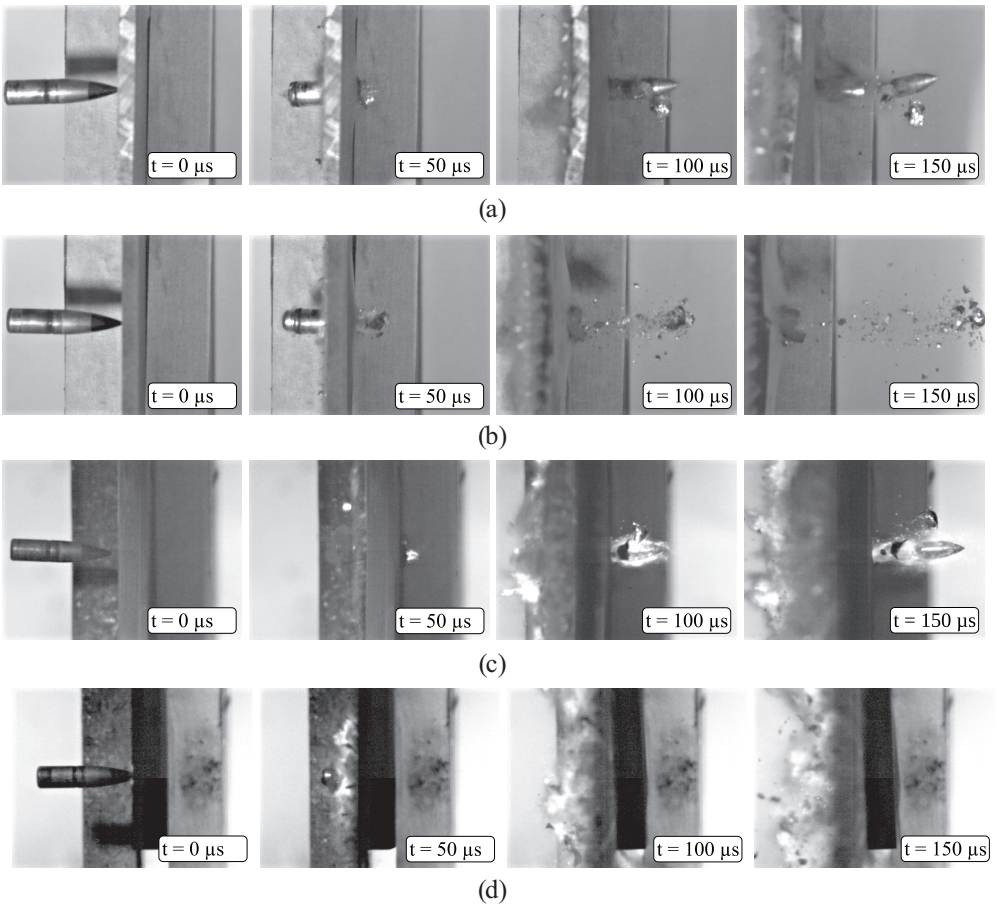

Figure 13. Timelapse of ballistic impacts of as-built and heat-treated monolithic plates with thicknesses of 5 and 10 mm. The projectile is the APM2 bullet in all cases: (a) 5 mm, as-built plate, $v_i = 526.7$ m/s; $v_r = 234.8$ m/s, (b) 5 mm, heat-treated plate, $v_i = 536.0$ m/s; $v_r = 62.1$ m/s, (c) 10 mm, as-built plate, $v_i = 705.3$ m/s; $v_r = 281.0$ m/s and (d) 10 mm, heat-treated plate, $v_i = 626.9$ m/s; $v_r = 0$.

allowing sufficient clearance for each test to be unaffected by preceding attempts, which allowed for a maximum of six shots in each 100 mm × 100 mm plate. However, due to frequent fragmentation and cracking of the material during impact, the number of tests in each plate were determined on a case-by-case basis.

The plates were weighed prior to testing and densities of 8034.4 and 8027.2 kg/m^3 were recorded for the as-built and the heat-treated materials, respectively. Measuring the plate thickness with a precision caliper found agreement with the nominal value of 5 mm to within 0.1 mm.

Results

Monolithic plates. Figure 13 shows representative time-lapses of the ballistic tests of as-built and heat-treated monolithic plates with thicknesses of 5 and 10 mm impacted by APM2 bullets. The initial and residual velocities, respectively v_{i} and v_{r}, are specified in the captions for each case. The brass jacket of the bullet was ripped off during impact in all tests, as is normal for

Table 4. Ballistic limit velocities for each target tested as predicted by the Recht-Ipson model, in metres per second.

Target	Material	Projectile	v_{bl} (m/s)
5 mm plate	As built	Full APM2 bullet	354.00
		Core only	376.10
	Heat-treated	Full APM2 bullet	475.08
		Core only	549.80
10 mm plate	As built	Full APM2 bullet	623.30
	Heat-treated	Full APM2 bullet	754.32
Profile	As built	Full APM2 bullet	473.70
	Heat-treated	Full APM2 bullet	541.30

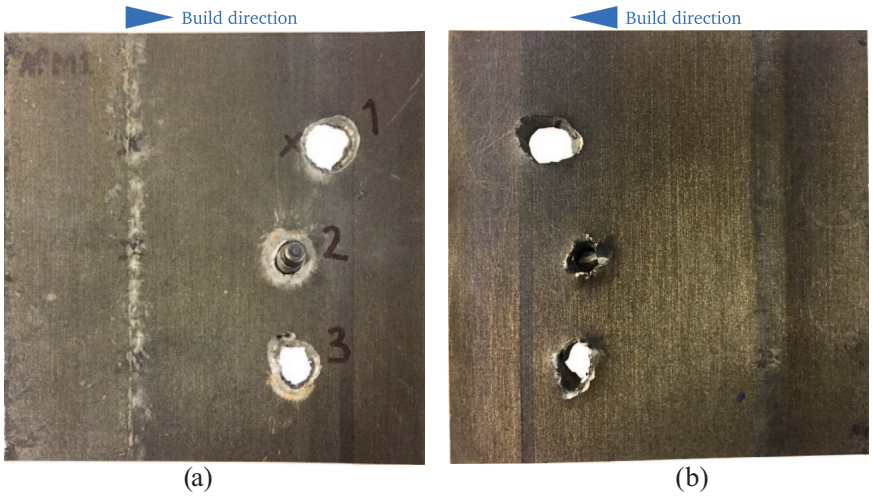

Figure 14. Photos of as-built 10 mm maraging steel plate after three tests at (1) 919.7 m/s, (2) 705.3 m/s and (3) 829.8 m/s: (a) front (bullet entrance) of the plate with a part of the bullet stuck in place and (b) back (bullet exit) of the plate.

high-strength steel targets (Holmen et al., 2017). Further, the hard steel cores broke in all tests where the bullet perforated the plate. This result is shown for the as-built plates in Figure 13(a) and (c), where the steel core broke into a small number of large pieces. In most cases for heat-treated plates, the projectile completely shattered during impact as exemplified by a 5 mm thick plate in Figure 13(b). In addition to shattering the bullet, the 10 mm thick plate was able to prevent any fragments from perforating as shown in Figure 13(d), and thus achieved the highest ballistic limit v_{bl} as listed in Table 4. It is worth noting that the yield stress of the bullet core was estimated to be 1200 MPa (Børvik et al., 2009), which is between the yield stress of the as-built and heat-treated material (Figure 6(a)).

Photographs of 10 mm thick as-built and heat-treated plates after testing are shown in Figures 14 and 15, respectively. The first notable difference between these was the seemingly higher ductility of the as-built plate compared with the heat-treated one. The perforation of the as-built plate in Figure 14 resembled ductile hole growth with tendencies to petalling on the exit side. The deformed and perforated zone was localised and there was no cracking, therefore these

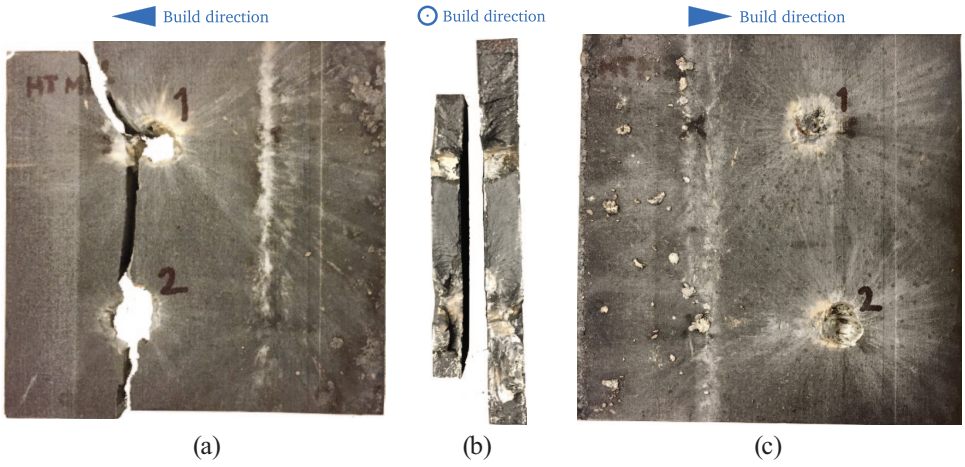

Figure 15. Photos of the heat-treated 10 mm maraging steel plates after shooting: (a) shows the plate fragmenting in two after tests at (1) 932.9 m/s and (2) 822.9 m/s and (b) surface of the fracture area and (c) shows bullets not able to perforate the plate at (1) 511.0 m/s and (2) 626.9 m/s.

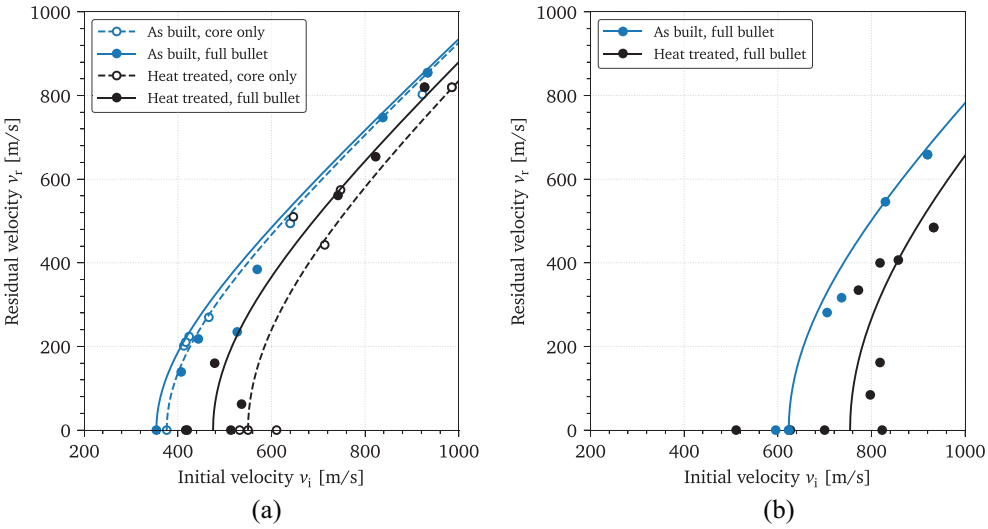

Figure 16. Ballistic limit curves of the monolithic plates: (a) 5 mm plates and (b) 10 mm plates.

plates were suitably reusable for multiple tests. This was not the case for the heat-treated plates, which were much more prone to cracking as illustrated by the pictures in Figure 15(a) and (b). Here, the first impact (1) at $v_i = 932.9$ m/s perforated the plate and created a large rugged hole with fragments detaching. During the second impact (2) at $v_i = 822.9$ m/s the plate cracked fully in two.

The fracture surface in Figure 15(a) was clearly normal to the print direction (hereafter referred to as 'print-line'), which according to the material tests had by far the lowest ductility (see Figure 6). The observation that cracks and breakages occurred along certain print-lines in

the plate depending on where the bullet struck is sufficient evidence to disregard the 'print-stop line' described in Section 2.2 as a cause for this effect. In the most extreme cases, the plate fully fractured and broke in two along the print-line as shown in Figure 15(a) where the plate was clamped along the print-line, allowing a large fragment (almost half the plate) to break away. This result sometimes occurred even without perforation. Thus, when a plate produced by SLM is loaded in all directions, fracture is expected to occur in the direction with the lowest ductility, that is primarily along the print-line. Fracture of this nature likely contributed to the large scatter observed in the residual velocities.

Initial and residual bullet velocities v_i and v_r were measured for each test. The Recht-Ipson (RI) model (Recht and Ipson, 1963) was fitted to the experimental data using the least squares method, thereby obtaining an estimate for the ballistic limit velocity v_{bl} for each of the three plate configurations. The RI model is given as:

$$v_r = a(v_i^p - v_{bl}^p)^{1/p}, \tag{4}$$

where a and p are constants derived from the conservation of energy and momentum for the projectile and target. For this study a and p were fixed at 1 and 2, respectively, despite that the mass of the plugs and fragments ejected during impact was not negligible, especially for the heat-treated plates. However, this assumption ensures the laws of conservation are obeyed and provides a consistent basis for comparison of v_{bl} for the plate variations. Furthermore, making accurate measurements of the mass of ejected fragments in order to estimate a and p would be difficult because of the large number of fragments produced. The resulting ballistic limit velocities for each plate configuration are presented in Table 4, while Figure 16 gives the ballistic limit curves of all monolithic plates. The scatter in results was considerable due to the brittle behaviour of the targets and as a consequence it was difficult to determine the ballistic limit velocity accurately from a limited number of tests. Thus, the ballistic limits in Table 4 should be considered approximate.

Figure 17 shows typical fracture surfaces inside the penetration channel of the as-built and heat-treated samples for the 5 mm monolithic plate. The top right close up image of the as-built sample in Figure 17(a) shows a crack in the fracture surface. This crack was parallel to the direction of the perforation, and small spherical particles – assumed to be residual unmolten powder from the SLM fabrication – can be observed at the bottom of the crack. Conversely, for the heat-treated sample the surface is smoother and no particles can be seen. It appears that fragments of the plate were torn off during penetration by the bullet, leaving a brittle fracture surface. This is shown in Figure 17(b), which also shows voids in the torn surface.

Profile plates. The profile plate targets were clamped so that the front panel of the plates was orthogonal to the bullet entry direction, and the inner structure was visible to the high-speed camera. This alignment conforms with the clamping area indicated for the monolithic plates in Figure 4(b). All target profile plates were able to fracture the hard steel core of the APM2 bullet to some extent, as can be seen in the timelapse in Figure 18(a). Figure 18(b) shows the most destructive case, where the bullet shattered and the profile plate was severely damaged, all the while preventing perforation. Like for the monolithic plates, the as-built material displayed a more ductile response than the heat-treated material, with comparatively very little fragmentation. Even though the bullet hole in the as-built material showed limited indication of ductile hole growth and only mild signs of petalling can be seen in Figure 19, the perforation process appeared to be ductile.

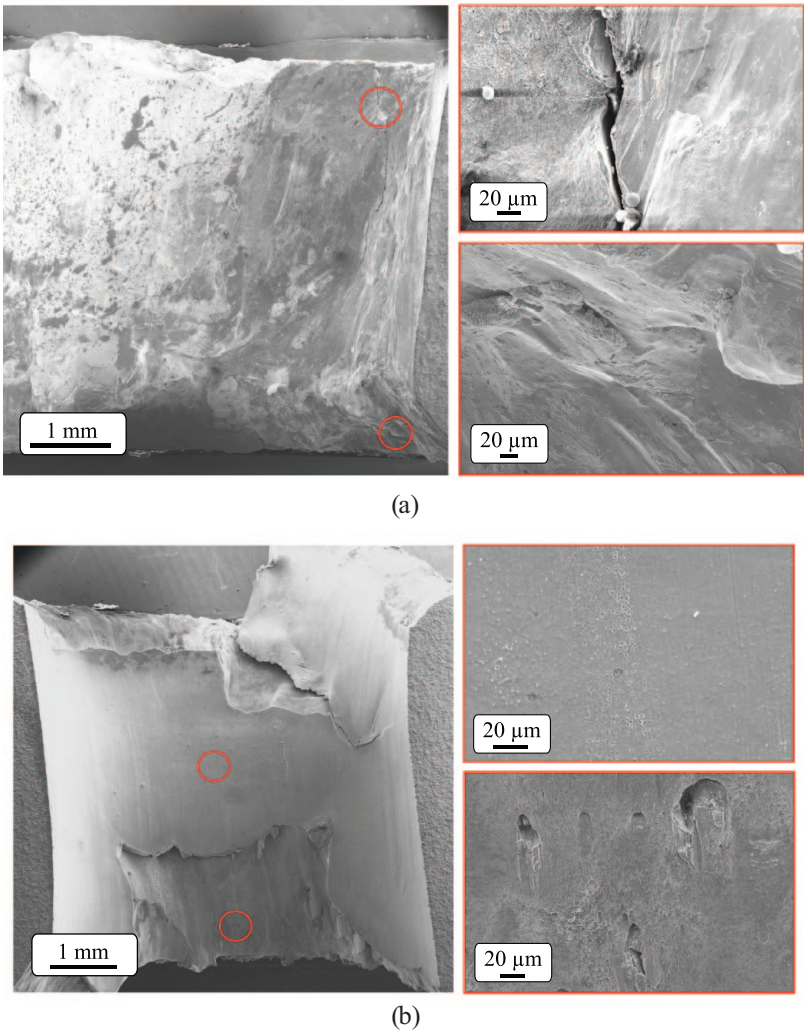

Figure 17. SEM images of the penetration channel in: (a) the as-built and (b) the heat-treated 5 mm monolithic plates (b), where the impact direction is from top to bottom. The images on the right show a close up of the area marked with a red circle on the left image.

The brittle nature of the heat-treated material became more evident for the profile plates. Figure 20 displays a heat-treated profile plate impacted at 926.6 m/s where there was significant damage to the inner corrugated structure and to the panel on the exit side – a crack running along the entire width of the specimen can be seen in Figure 20(c). The level of destruction rendered these plates unsuitable for additional tests, thereby limiting the number of data points compared to the as-built material.

The fit of the Recht-Ipson model to the experimental results is shown in Figure 21, with a considerable scatter of the results. Some of the tests were discounted from the fit due to the bullet impacting the plate in the corner of the profile rather than the centre, or the bullet exiting the same hole as a previous test. The resulting ballistic limit velocities for each profile are included in Table 4. The estimated ballistic limit of the profile plates was, as expected, between that of the two monolithic plates (Wadley et al., 2013).

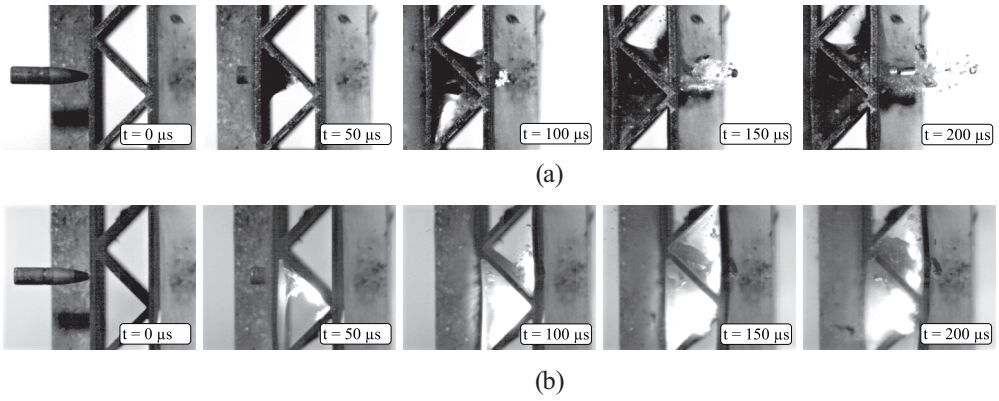

Figure 18. Profiles timelapse of ballistic tests: (a) as-built and (b) heat-treated.

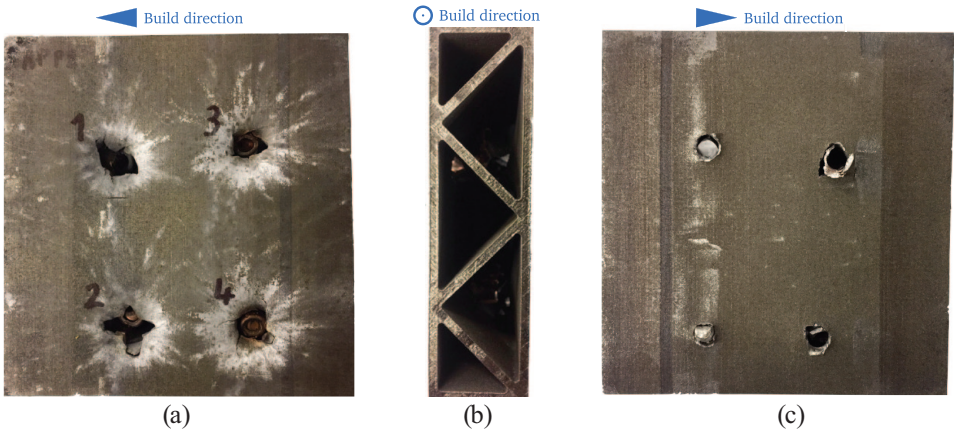

Figure 19. Photos of the as-built profile plates after four tests at (1) 540.3 m/s, (2) 489.7 m/s, (3) 476.7 m/s and (4) 480.0 m/s: (a) front (bullet entrance) of the plate, (b) side of the plate and (c) back (bullet exit) of the plate.

Summary and discussion

While the utility of employing AM to create intricate geometries tailored to fill gaps in material property space has been made clear (Ashby, 2013), the material properties arising from the process are still under investigation. This applies to both as-built and heat-treated material. The anisotropy may range from small (Meneghetti et al., 2017) to considerable (Mooney et al., 2019) in as-built AM maraging steel. In this study a clear anisotropy was found in the material, to some extent for the yield stress $\sigma_{0.2}$ (highest in the 45° direction) but most considerably for the fracture strain. The as-built material was very ductile in the 90° direction, reaching true strain levels of 0.7 and more as seen in Figures 6(a) and 7(b) and Table 3. This direction also had the lowest scatter levels. A fairly brittle behaviour was noted for the 0° and 45° directions, between which it was difficult to draw any clear distinctions due to the scatter. Weak zones created by the presence of large particles revealed by the CT scan in Figure 11 likely contributed to this scatter. Altering the scan strategy or the laser settings may increase the relative density (Mooney and Kourousis, 2020). How

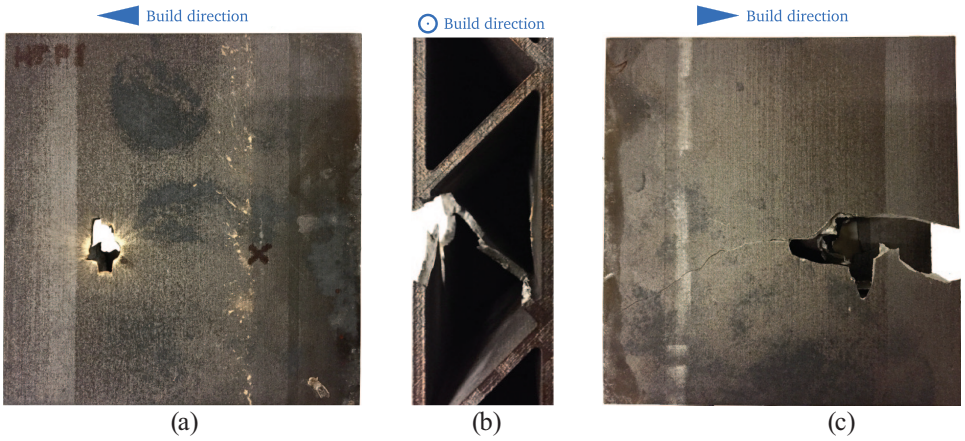

Figure 20. Photos of the heat-treated profile plates after one test at 926.6 m/s: (a) front (bullet entrance) of the plate, (b) side of the plate and (c) back (bullet exit) of the plate.

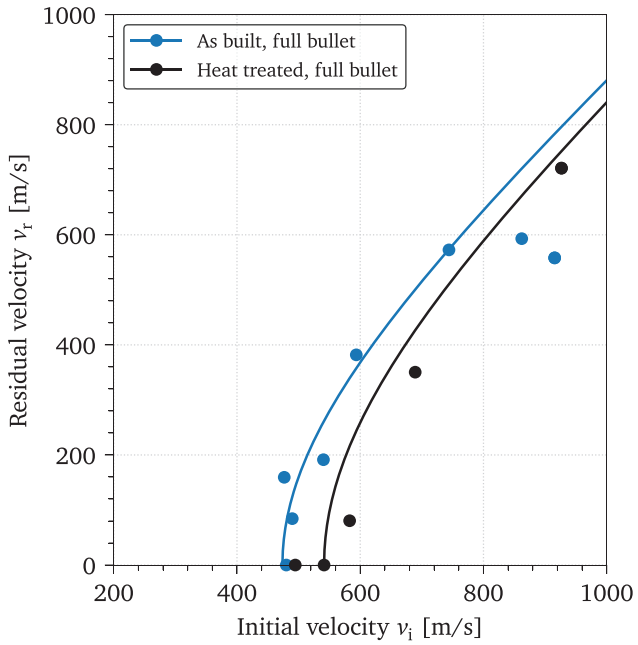

Figure 21. Ballistic limit curves for the tested profiles with Recht-Ipson model parametres $a = 1$ and $p = 2$.

the material anisotropy affects the performance of the plates during ballistic impact is difficult to quantify experimentally because of the multiaxial stress states in the plates during impact. However, simulations of ballistic impact against 5 mm thick AlSi10Mg AM plates showed that calibrating the constitutive relation based on the 90° results gave better results in terms of ballistic limit velocity compared with calibrations based on the 0° and 45° directions (Kristoffersen et al., 2020). Whether this is true for this material remains to be seen, but it seems likely.

After heat treatment, $\sigma_{0.2}$ increased significantly from around 1100 MPa to approximately 2000 MPa. This increase was accompanied by a severe reduction of ductility, and there was still notable scatter. The 90° specimens clearly had the lowest scatter for the as-built material, but after heat treatment the scatter was now similar to the other two directions, and most markedly for the fracture strain. The SHTB tests of the as-built material showed that the strain rate sensitivity was low and approximately the same in all directions. Increasing the strain rate seemingly lowered the scatter, possibly because there is less time for the material to distribute the load assuming that the voids observed in for example Figure 11 act as cracks. Based on simulations (Eibl and Curbach, 1989), dynamic loading appears to engage more of the material behind a crack tip whilst a static load leads to higher stress concentration.

The ballistic impact tests showed that the heat treatment increased the ballistic limit velocity noticeably. For the 5 mm monolithic plates, the increase was approximately 25%. The as-built plates had clear signs of ductile hole growth and petalling in Figure 14, and the heat-treated plates either stopped and shattered the bullet or tended to fragment (illustrated in Figure 15), leaving a completely different fracture surface as depicted in Figure 17. Reflecting the tensile test results, the heat-treated plates showed more scatter than the as-built ones as plotted in Figure 16. This scatter makes it difficult to draw any robust conclusions regarding the difference between using the full APM2 bullet and the core only. Modifying the heat treatment for optimum perforation resistance is a natural possibility for further research.

Doubling the plate thickness to 10 mm predictably increased the ballistic limit velocity (see Table 4 and Figure 16); an increase of over 60% was achieved for both as-built and heat-treated plates. This result is quite interesting given that a 60% increase in velocity more than doubles the kinetic energy of the bullet. The as-built plates absorbed the energy by plastic deformation to a larger extent than the heat-treated plates, which showed a high degree of fragmentation. The effect of the heat treatment in terms of v_{bl} was less for the 10 mm plates than for the 5 mm plates. Further, the hard steel core of the bullet was often severely damaged, ranging from breaking into large pieces for 5 mm as-built plates to complete obliteration for some 5 mm and all 10 mm heat treated plates. Previous work on perforation of 12 mm thick high-strength steel plates (two layered 6 mm plates) recorded only minor damage to the armour piercing bullet (Børvik et al., 2009). The ballistic tests thus showed a remarkable potential for AM maraging steel in protective structures.

Increasing the thickness of steel targets beyond 10 mm has been demonstrated to provide notable gains in terms of v_{bl} (Børvik et al., 2003). Increasing the thickness of the AM maraging steel plates beyond 10 mm would result in better perforation resistance. An investigation that combines the geometric possibilities of AM with the ultra-high strength of maraging steel (or even combinations of materials) using multi-objective numerical optimisation (Cid-Montoya et al., 2015) could drastically improve the ballistic limit velocity and spawn a whole new class of protective structures by use of architectural design (Fleck et al., 2010). Further research along these lines would be of great interest to the impact engineering community.

A simple profile plate with the same areal density as the 10 mm plates was also built and tested. Using this truss-like structure rather than a monolithic 10 mm plate proved deleterious to the perforation resistance. Again the as-built plates were comparatively ductile. The APM2 bullet caused significant damage to the heat-treated plates, evident in Figure 20. Again the hard steel core of the bullet was broken despite the even lower thickness of the profile plates. The shattering of the steel core may be caused by extremely high magnitude stress waves arising upon impact against the extremely hard heat-treated plates with much higher yield stress. More complex geometries, like optimised gyroids, lidinoids or other advanced shapes, remain to be investigated.

Concluding remarks

The ballistic properties of a selective laser melting additive manufactured maraging high-strength steel were investigated. The material was tested in as-built and heat-treated configurations in the form of monolithic plates and truss-like profiles, and the following conclusions were drawn:

- After heat treatment at 490 °C for 6 h, the yield stress of the material was approximately doubled compared to that of the as-built material. Conversely, the ductility was drastically reduced.
- Ballistic testing of as-built and heat-treated plates showed the significant potential of this material for protective applications. The resistance of the samples was such that the high-strength steel core of the armour-piercing bullet shattered in many tests, in spite of the relatively low thickness of the target plates.
- Heat treatment increased the ballistic limit of the tested targets in all configurations. However, the heat-treated targets were more prone to cracking and fragmentation, and therefore did not withstand as many shots as the as-built plates, which displayed a more ductile behaviour. This is in agreement with the results of the tensile tests.
- A significant scatter was found in both the tensile and ballistic properties. Relatively large voids and particles were found in the additive manufactured maraging steel samples, which were most likely responsible for the scattered results. These large particles were investigated and it was shown that heat treatment did not alleviate the problem.

To conclude, this work demonstrated the potential of selective laser melting maraging steel in protective applications. However, we believe that there is room for improvement regarding the strength – ductility trade-off for this material, especially through minimising the presence of larger voids and particles. Moreover, the heat treatment could be optimised to find a balance between strength and ductility, and in turn significantly improve the ballistic performance of the material.

Acknowledgements

The authors would like to acknowledge Mr. Trond Auestad, Mr. Tore Andre Kristensen and Mr. Tore Wisth for assistance with the various experimental programmes, and Dr. Susanne Thomesen and Mr. Ole Tore Buset for the help with the microscopy and CT scanner.

Data availability

The raw/processed data required to reproduce these findings cannot be shared at this time as the data also forms part of an ongoing study.

Declaration of conflicting interests

The author(s) declared no potential conflicts of interest with respect to the research, authorship, and/or publication of this article.

Funding

The author(s) disclosed receipt of the following financial support for the research, authorship, and/or publication of this article: The present work has been carried out with financial support from Centre of Advanced Structural Analysis (CASA), Centre for Research-based Innovation, at the Norwegian University of Science and Technology (NTNU) and the Research Council of Norway through project no. 237885 (CASA). Ms. Maisie Edwards-Mowforth has worked under an Erasmus scholarship.

ORCID iD

Miguel Costas https://orcid.org/0000-0002-0117-6978

References

Akram J, Chalavadi P, Pal D, et al. (2018) Understanding grain evolution in additive manufacturing through modeling. *Additive Manufacturing* 21: 255–268.

Ashby M (2013) Designing architectured materials. *Scripta Materialia* 68(1): 4–7.

Bai Y, Wang D, Yang Y, et al. (2019) Effect of heat treatment on the microstructure and mechanical properties of maraging steel by selective laser melting. *Materials Science and Engineering A* 760: 105–117.

Bai Y, Yang Y, Wang D, et al. (2017) Influence mechanism of parameters process and mechanical properties evolution mechanism of maraging steel 300 by selective laser melting. *Materials Science and Engineering A* 703: 116–123.

Børvik T, Burbach A, Langberg H, et al. (2008a) On the ballistic and blast load response of a 20ft ISO container protected with aluminium panels filled with a local mass—phase II: Validation of protective system. *Engineering Structures* 30(6): 1621–1631.

Børvik T, Hanssen A, Dey S, et al. (2008b) On the ballistic and blast load response of a 20 ft ISO container protected with aluminium panels filled with a local mass Phase I: Design of protective system. *Engineering Structures* 30(6): 1605–1620.

Børvik T, Clausen AH, Eriksson M, et al. (2005) Experimental and numerical study on the perforation of AA6005-T6 panels. *International Journal of Impact Engineering* 32: 35–64.

Børvik T, Dey S and Clausen AH (2009) Perforation resistance of five different high-strength steel plates subjected to small-arms projectiles. *International Journal of Impact Engineering* 36(7): 948–964.

Børvik T, Hopperstad OS, Langseth M, et al. (2003) Effect of target thickness in blunt projectile penetration of weldox 460 e steel plates. *International Journal of Impact Engineering* 28(4): 413–464.

Børvik T, Langseth M, Hopperstad OS, et al. (1999) Ballistic penetration of steel plates. *International Journal of Impact Engineering* 22(9–10): 855–886.

Casati R, Lemke JN, Tuissi A, et al. (2016) Aging behaviour and mechanical performance of 18-Ni 300 steel processed by selective laser melting. *Metals* 6: 218.

Chen W and Song B (2011) *Split Hopkinson (Kolsky) Bar. Design, Testing and Applications*. New York, NY: Springer.

Chen Y, Clausen AH, Hopperstad OS, et al. (2011) Application of a split-hopkinson tension bar in a mutual assessment of experimental tests and numerical predictions. *International Journal of Impact Engineering* 38(10): 824–836.

Cid-Montoya M, Costas M, Díaz J, et al. (2015) A multi-objective reliability-based optimization of the crashworthiness of a metallic-GFRP impact absorber using hybrid approximations. *Structural and Multidisciplinary Optimization* 52(4): 827–843.

Conde FF, Escobar JD, Oliveira JP, et al. (2019) Effect of thermal cycling and aging stages on the microstructure and bending strength of a selective laser melted 300-grade maraging steel. *Materials Science and Engineering A* 758: 192–201.

Demir T, Übeyli M and Yıldırım RO (2008) Investigation on the ballistic impact behavior of various alloys against 7.62mm armor piercing projectile. *Materials & Design* 29(10): 2009–2016.

Eibl J and Curbach M (1989) An attempt to explain strength increase due to high loading rates. *Nuclear Engineering and Design* 112: 45–50.

Fagerholt E, Børvik T and Hopperstad OS (2013) Measuring discontinuous displacement fields in cracked specimens using digital image correlation with mesh adaptation and crack-path optimization. *Optics and Lasers in Engineering* 51(3): 299–310.

Fleck NA, Deshpande VS and Ashby MF (2010) Micro-architectured materials: Past, present and future. *Proceedings of The Royal Society A Mathematical Physical and Engineering Sciences* 466(2121): 2495–2516.

Forrestal MJ, Børvik T, Warren TL, et al. (2014) Perforation of 6082-T651 aluminum plates with 7.62 mm APM2 bullets at normal and oblique impacts. *Experimental Mechanics* 54: 471–481.

Frazier WE (2014) Metal additive manufacturing: A review. *Journal of Materials Engineering and Performance* 23(6): 1917–1928.

Gorsse S, Hutchinson C, Gouné M, et al. (2017) Additive manufacturing of metals: A brief review of the characteristic microstructures and properties of steels, Ti-6Al-4V and high-entropy alloys. *Science and Technology of Advanced Materials* 18(1): 584–610.

Harris JA, Winter RE and McShane GJ (2017) Impact response of additively manufactured metallic hybrid lattice materials. *International Journal of Impact Engineering* 104: 177–191.

Holmen JK, Solberg JK, Hopperstad OS, et al. (2017) Ballistic impact of layered and case-hardened steel plates. *International Journal of Impact Engineering* 110(9): 4–14.

ISO/ASTM. 52900:2018-06 (2018) Additive manufacturing general principles terminology.

Jägle EA, Choi P-P, Van Humbeeck J, et al. (2014) Precipitation and austenite reversion behavior of a maraging steel produced by selective laser melting. *Journal of Materials Research* 29(17): 2072–2079.

Jägle EA, Sheng Z, Kürnsteiner P, et al. (2016) Comparison of maraging steel micro- and nanostructure produced conventionally and by laser additive manufacturing. *Materials* 10(1): 1–15.

Kasilingam S, Iqbal MA and Senthil R (2019) Influence of impactor nature, mass, size and shape on ballistic resistance of mild steel and armox 500 T steel. *International Journal of Protective Structures* 10(2): 174–197.

Kempen K, Yasa E, Thijs L, et al. (2011) Microstructure and mechanical properties of selective laser melted 18Ni-300 steel. *Physics Procedia* 12: 255–263.

Kim D, Kim T, Ha K, et al. (2020) Effect of heat treatment condition on microstructural and mechanical anisotropies of selective laser melted maraging 18Ni-300 steel. *Metals* 10(3): 410.

Kristoffersen M, Costas M, Koenis T, et al. (2020) On the ballistic perforation resistance of additive manufactured AlSi10Mg aluminium plates. *International Journal of Impact Engineering* 137: 103476.

Ma CY and Liew JYR (2013) Blast and ballistic resistance of ultra-high strength steel. *International Journal of Protective Structures* 4(3): 379–413.

Madhu V and Bhat T (2011) Armour protection and affordable protection for futuristic combat vehicles. *Defence Science Journal* 61(4): 394–402.

Masood S, Ruan D and Rajapatruni P (2018) Mechanical performance of plymetal structures subjected to impact loading. *International Journal of Protective Structures* 9(1): 65–76.

Meneghetti G, Rigon D, Cozzi D, et al. (2017) Influence of build orientation on static and axial fatigue properties of maraging steel specimens produced by additive manufacturing. *Procedia Structural Integrity* 7(149): 149–157.

Mooney B and Kourousis K (2020) A review of factors affecting the mechanical properties of maraging steel 300 fabricated via laser powder bed fusion. *Metals* 10(9): 1273.

Mooney B, Kourousis KI and Raghavendra R (2019) Plastic anisotropy of additively manufactured maraging steel: Influence of the build orientation and heat treatments. *Additive Manufacturing* 25(19): 19–31.

Ngo TD, Kashani A, Imbalzano G, et al. (2018) Additive manufacturing (3D printing): A review of materials, methods, applications and challenges. *Composites Part B Engineering* 143: 172–196.

Ranaweera P, Weerasinghe D, Fernando P, et al. (2020) Ballistic performance of multi-metal systems. *International Journal of Protective Structures* 11(3): 379–410.

Recht RF and Ipson TW (1963) Ballistic perforation dynamics. *Journal of Applied Mechanics* 30: 384–390.

Tan C, Zhou K, Ma W, et al. (2017) Microstructural evolution, nanoprecipitation behavior and mechanical properties of selective laser melted high-performance grade 300 maraging steel. *Materials & Design* 134: 23–34.

Vock S, Klöden B, Kirchner A, et al. (2019) Powders for powder bed fusion: A review. *Progress in Additive Manufacturing* 4: 383–397.

Vyatskikh A, Delalande S, Kudo A, et al. (2018) Additive manufacturing of 3D nano-architected metals. *Nature Communications* 9: 593–598.

Wadley HN, Dharmasena KP, O'Masta MR, et al. (2013) Impact response of aluminum corrugated core sandwich panels. *International Journal of Impact Engineering* 62: 114–128.

Yasa E, Kempen K and Kruth J (2010) Microstructure and mechanical properties of Maraging Steel 300 after selective laser melting. In: Proceedings of the solid freeform fabrication symposium, Austin, TX, 9–11 August, pp.383–396.

Yin S, Chen C, Yan X, et al. (2018) The influence of aging temperature and aging time on the mechanical and tribological properties of selective laser melted maraging 18Ni-300 steel. *Additive Manufacturing* 22: 592–600.

Zipperian D (2010) *Metallographic Handbook*. Tucson, AZ: PACE Technologies. p.189.